



**HAL**  
open science

## Nano-spheroid formation on YAG surfaces induced by single ultrafast Bessel laser pulses

Tianqu Chen, Guodong Zhang, Hao Zhang, Jing Lv, Yuheng Wang, Pubo Qu, Razvan Stoian, Guanghua Cheng

► **To cite this version:**

Tianqu Chen, Guodong Zhang, Hao Zhang, Jing Lv, Yuheng Wang, et al.. Nano-spheroid formation on YAG surfaces induced by single ultrafast Bessel laser pulses. *Applied Surface Science*, 2022, 604, pp.154360. 10.1016/j.apsusc.2022.154360 . ujm-03753502

**HAL Id: ujm-03753502**

**<https://ujm.hal.science/ujm-03753502>**

Submitted on 19 Aug 2022

**HAL** is a multi-disciplinary open access archive for the deposit and dissemination of scientific research documents, whether they are published or not. The documents may come from teaching and research institutions in France or abroad, or from public or private research centers.

L'archive ouverte pluridisciplinaire **HAL**, est destinée au dépôt et à la diffusion de documents scientifiques de niveau recherche, publiés ou non, émanant des établissements d'enseignement et de recherche français ou étrangers, des laboratoires publics ou privés.

# Nano-Spheroid Formation on YAG Surfaces Induced by Single Ultrafast Bessel Laser Pulses

Tianqu Chen<sup>1,2</sup>, Guodong Zhang<sup>1</sup>, Hao Zhang<sup>1</sup>, Jing Lv<sup>1</sup>, Yuheng Wang<sup>3</sup>, Pubo Qu<sup>4</sup>, Razvan Stoian<sup>5</sup>, Guanghua Cheng<sup>1,\*</sup>

<sup>1</sup>*School of Artificial Intelligence, Optics and Electronics (iOPEN), Northwestern Polytechnical University, Xi'an 710072, China*

<sup>2</sup>*Department of Communication Science and Engineering, Fudan University, Shanghai 200438, China*

<sup>3</sup>*Research Center of Semiconductor Lighting and Information Engineering Technology, South China University of Technology, Guangzhou 510641, China*

<sup>4</sup>*School of Artificial Intelligence, Henan University, Kaifeng 475001, China*

<sup>5</sup>*Laboratoire Hubert Curien, UMR 5516 CNRS, Université Jean Monnet, 42000 Saint Etienne, France*

\*Corresponding author: [guanghuacheng@nwpu.edu.cn](mailto:guanghuacheng@nwpu.edu.cn)

**ABSTRACT:** We report on single pulse ultrafast Bessel laser beam processing of YAG ceramic surfaces as a method for producing contamination-free submicron particles and size adjustable surface hemisphere structures of different curvature signs. The micro-machining process was performed in both air and liquid environments, leading to a variety of surface structures depending on the processing parameters. Particularly, a transformation of the surface structure morphology from micro-hole profiles to hemisphere extrusions was observed. The size of the hemisphere structure is found to be highly sensitive to laser parameters, such as pulse energy, pulse duration and beam focusing position. Through careful analyses of the influence of the laser pulse parameters, a precise regulation of the lateral diameter and height of the hemisphere structure was achieved. Large area hemisphere arrays with low standard deviation in size were fabricated. The detachment of the emerging structures and subsequent particle deposition can be observed in liquid environments when the height-diameter aspect ratio of the hemisphere exceeds a factor of 0.65. The mechanisms for the formation and morphology features of the hemisphere structure are discussed with cross-sectional and morphology imaging via Scanning Electron Microscopy and Atomic Force Microscopy. As a preliminary step towards submicron particle generation in liquid environments, the observation of surface hemispheres has interest in exploring the initial mechanisms of particles formation under laser ablation in liquids. The presented method allows for the fabrication of contamination-free and size adjustable YAG submicron convex structures which have potential applications in integrated optics, biotechnology and other advanced processing techniques.

**Keywords:** Ultrafast laser; Bessel beam; Liquid assisted processing; Surface structure; Nano-Spheroid

## INTRODUCTION

Ultrafast laser processing has been the subject of thriving research for decades due to its unique features, such as a high flexibility for two- and three-dimensional selective writing, a wide range of machinable materials and a high processing resolution [1-5], with the prospect of bypassing the

1 diffraction limit. Conventional laser ablation and direct writing methods based on material  
2 subtraction can be utilized in manufacturing surface and volume topographical and morphological  
3 features in the form of craters while with variable aspect shapes, grooves, void spaces, and  
4 nano-hole structures, allowing via their space arrangements and scale to generate new functions  
5 and to enable novel applications [6-10].  
6

7 In addition, intrinsically related to the ablative processes but not exclusively relying on  
8 subtractive features, other profiles and structures including micro- and nano-particles and surface  
9 bumps can also be obtained in various materials using similar laser processing methods [11-16].  
10 These processes rely on the accurate control of not only the material removal process but also the  
11 ablation byproducts. The standard laser processing involves local energy deposition which is  
12 normally induced by nonlinear character, heating, phase transformation, ablation and material  
13 removal. Determined by the optical skin depth and thermal transport, the heating profile becomes  
14 inhomogeneous, leading to a range of ablation products in the form of plasma plumes and debris  
15 of various sizes. A typical thermodynamic trajectory of the excited material includes evolution in  
16 the range of the critical point where indicate material features can transform through the mixed  
17 phase region or evolution in the vicinity of the binodal. The consequences for processing are  
18 manifold [17,18].  
19

20 In subtractive conditions, concave profiles can be easily fabricated on the surface of the  
21 substrate when the material ablation occurs. On the other hand, nanoscale aggregates can form in  
22 the cooling plasmas by coalescence and aggregation [19]. In between, accurate controls of the  
23 hydrodynamic trajectory of the hot material, its evacuation, and its rapid cooling can determine a  
24 multitude of topography profiles and curvature signs of the structured surfaces. The results can be  
25 related to the local pressure driving the material pull-out and to the confinement environment  
26 around. Relevant conditions often involve control of the energy distribution via e.g. the distance  
27 between focusing region and substrate surface or the presence of denser, liquid environments. A  
28 regulated hydrodynamic expansion and quenching will give extended flexibility to design  
29 structural profiles and, notably, convex structures can thus be obtained. Here as well liquid  
30 environments can be demonstrated to be effective in regulating process hydrodynamics, in a way  
31 similar to its influence in the techniques of nanoparticle production by pulsed laser ablation (PLA)  
32 where it influences condensation, coalescence nucleation and growth in the plasma phase. As a  
33 consequence, splitting particles in the sub- $\mu\text{m}$  range and surface extrusions can be generated  
34 following the hydrodynamic behavior of molten material ejection in PLA in liquid (PLAL)  
35 environments [20].  
36

37 The interest in surface extrusion profiles can be significant and we review below some of the  
38 formation drivers. A first potential driver lies in surface deformation by excitation below the  
39 surface [15]. This excitation can result in local micro-explosions or just following local  
40 thermomechanical expansion upon confined heating. Furthermore, a combination of stress and  
41 melting can generate extrusions and particle jetting [21]. Previous laser processing works have  
42 also obtained various convex or particle structures [22]. Formation mechanism of these structures  
43 mostly relies on the evolution of liquid regions, flow and rapid quenching and pressure relaxation  
44 within the laser affected region. In order to induce adequate molten material, the volume of the  
45 laser-material interaction region is designed to be large enough. For experiments with  
46 conventional CW Gaussian beams, an accurate control of the focal position along the propagation  
47 direction is necessary, while complex nonlinear multi-pulse interactions combined with  
48  
49  
50  
51  
52  
53  
54  
55  
56  
57  
58  
59  
60  
61  
62  
63  
64  
65

unsatisfactory precision and processing efficiency are involved.

Here a new technique is proposed relying on picosecond and femtosecond single pulse Bessel laser beam for convex structures fabrication. By introducing a liquid processing environment, this method can be utilized for both high quality surface convex structure and micro-particles fabrication by simply varying the laser focal depth.

Comparing to Gaussian laser beam, the Bessel-Gauss beam, which can be directly obtained by using an axicon, has a much longer focusing distance under the same focusing condition [23]. The Non-diffractive feature of the Bessel beam together with its self-healing property are known to maintain a constant intensity over large propagation distances in various environments (air and liquid and interface) [24-26].

Utilization of Bessel beam can offer a more accurate control considering its unique nature of standing pattern. Bessel beam is gradually constructed by the side photons and its construction time is related to the projection of the corresponding k-vectors on the axis [26, 27]. The relaxation being perpendicular to the axis (as following the direction of the highest gradient) would have as consequence smoother relaxation condition along the axis and therefore a larger range for generating spheroids by controlling the evacuation of the liquids. The state of the liquid is also better controlled (and thus its viscosity) by the standing pattern generated by conical refraction and side-replenishment by photons as in case of a propagative wave-packet [12-14, 26-28].

With the microexplosion, melt material therefore can be ejected out if the micro-hole is induced near the surface while cavitation occurs in the volume. The pressure relaxation process follows the geometry extended in the longitudinal direction, with a stronger relaxation drive in the radial direction [27]. By precisely adjusting the beam focusing depth, the molten material can be trapped at the surface exit, creating an spherical extrusion. Precise dimensional control of the convex structure can thus be realized. Comparing to multi-pulse Gaussian beams, processing with single pulse Bessel beam can simplify the formation of convex structures, optimize structure accuracy and increase processing efficiency. Therefore, our method of using single-shot Bessel beams has great advantages in simplifying the technique and is expected to better reveal the formation processes of convex structures.

## **MATERIAL AND METHODS**

A complete description of the experimental setup used in this study is detailed in one of our earlier works [24]. A simplified schematic setup of the Bessel beam ablation system is shown in Figure.1. A 178 ° axicon and a 4f system (demagnification factor 40) are used to obtain a focused Bessel beam (with 1030 nm central wavelength and 0.2 - 25 ps adjustable pulse duration). The final Bessel beam after the 4f system has a half-cone angle of 19.5° in air and about 11.1° inside the YAG ceramic substrate. The central lobe diameter of the Bessel beam is about 2.14 μm on the YAG ceramic. Accordingly the diameter of the zero-order Bessel beam is about 1 μm at 1/e<sup>2</sup> intensity. The same optics are used for the laser processing in water. A cuboid fused silica cell filling with distilled water serves as a sample cell. YAG ceramic sample was immersed into the distilled water at a 2 mm depth, and a high transmittance 1 mm thick glass slide was used to keep the surface of the water stable when the sample was moving. Between the glass slide and the YAG ceramic sample there is a 2 mm gap for protecting the glass slide from laser damage.

The nondiffractive length of the focusing Bessel beam in air was calculated to be around 600 μm. The polished bulk YAG ceramic sample was fixed on a three-dimension air-bearing

translation stage in order to precisely control the relative movement with respect to the laser beam. Scanning electron microscope (SEM) and atomic force microscope (AFM) were employed to image the surface micro-structures induced by single pulse Bessel beams with various laser parameters. Focused Ion beam (FIB) milling was used to reveal the longitudinal cross-sectional morphology of the fabricated structures. Nonlinear processes involving the interaction between transparent materials and matter are sensitive to the pulse duration and energy. A series of experiments have been conducted to investigate the configurations of the ablation configuration under pulse durations from 0.25 ps to 6.0 ps.

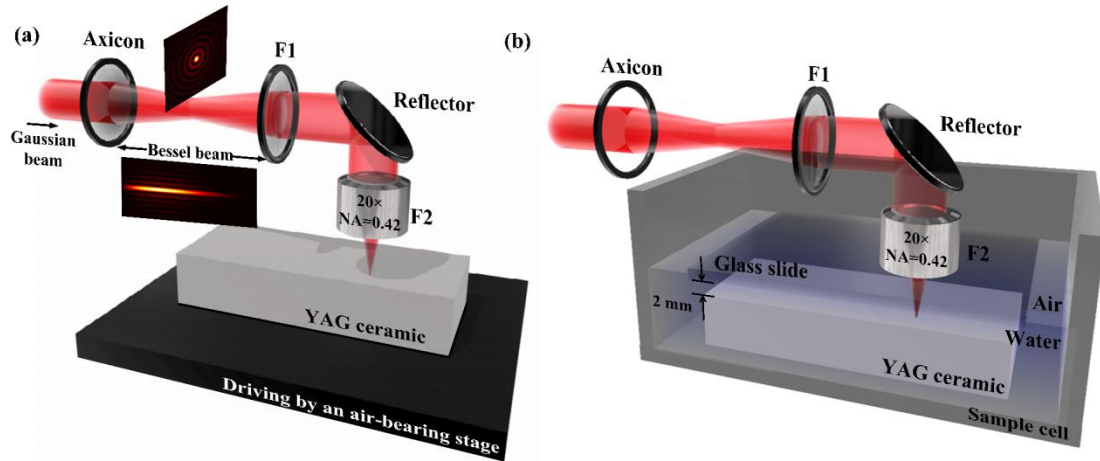


**Figure 1.** (a) A schematic of the setup used for the Bessel beam processing of a YAG ceramic target in air. (b) A schematic of the setup used for the Bessel beam processing with distilled water.

The Morphology of the surface micro-structures depends therefore strongly on the laser energy and on the pulse duration. At a given energy in the accessible range, submicron holes can only be induced by beams with short pulse duration ( $< 2.5$  ps), which is similar to the case in fused silica and aluminosilicate glass (Gorilla glass, corning). With the increase of pulse duration, central holes are replaced by hemisphere structures which have similar diameters as the holes. Figure 2 distinguishes the hemisphere structures and other depressed structures, acting as a frontier between two different hydrodynamic regimes enabled by the laser radiation: complete material ejection and quenched material advance. As the results depicted, hemisphere structures can only be constructed with pulse duration longer than 2.5 ps and pulse energy larger than  $1,401 \text{ J/cm}^2$  ( $11 \mu\text{J}$ ). Molten material is ejected from the hole and resolidifies on the surface in Figure 2b. This morphology is a strong indication that the formation mechanism of this structure is highly related to the thermal and thermomechanical effects occurred in laser processing, notably in the distribution of heat and pressure along the propagation axis within the bulk.

The gradual transformation from concave micro-hole to convex hemisphere as shown in the 2.5 ps condition indicate that the hemisphere is constructed by the internal molten material advance. This type of combination of mechanical pressure and fluid dynamics was observed in other circumstances on a range of materials from metal films to glasses [29-31]. The use of the non-diffractive beams offers nevertheless an additional control knob in positioning the thermomechanical source with respect to the surface, delivering a softer pressure relaxation path in the axial direction compared to the radial one. By controlling the relative position between laser irradiate area and substrate surface, different structures from protrusion to hemisphere can be

obtained.

## RESULT AND DISCUSSION

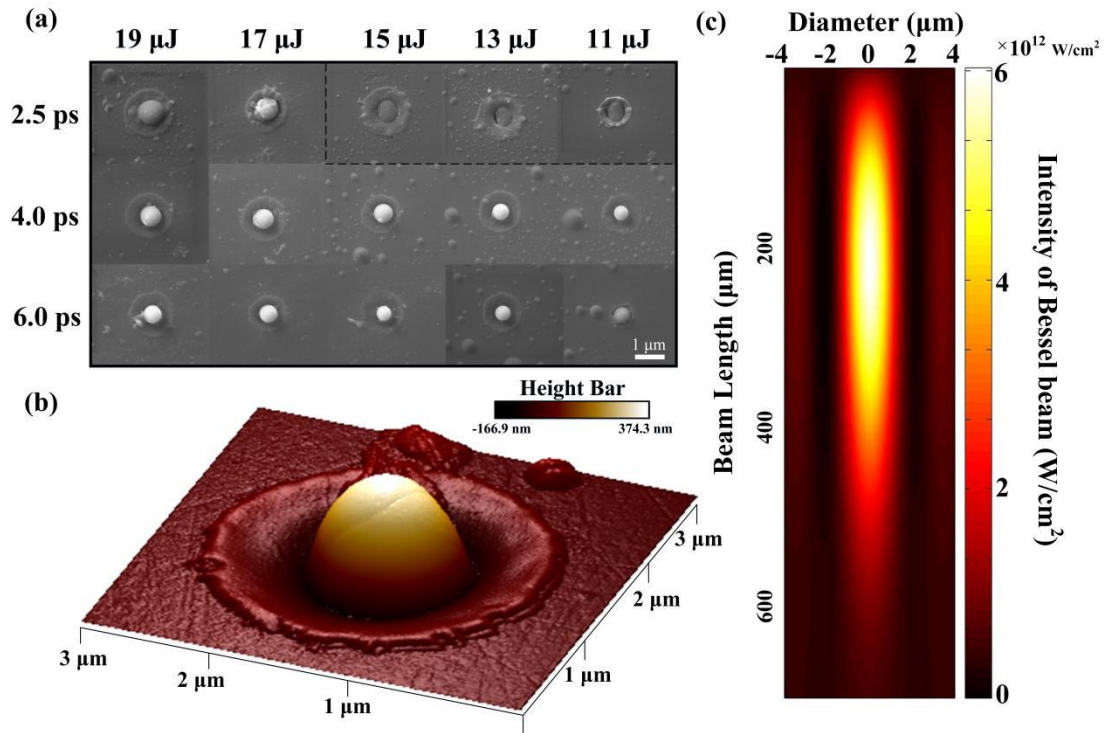


**Figure.2** (a) SEM images of surface micro-structures induced by single pulse Bessel beams with different laser parameters. Focusing depth of the beam remains unchanged. Scale bar is 1  $\mu\text{m}$ . (b) is AFM image of one semi-sphere on YAG ceramic surface written by a 17  $\mu\text{J}$  with 4 ps pulse. (c) the intensity distribution of ultrafast Bessel laser beam in xz plane.

In comparison with fused silica and aluminosilicate glass (Gorilla), the processing window in YAG ceramic is the biggest to trigger protrusion structure on surface. Smooth hemisphere can be obtained just on the YAG ceramic. There are equally specific material features of the YAG ceramic that favors this behavior compared to other dielectric materials. We note that the thermal expansion coefficient of liquid YAG at high temperature ( $2.21 \times 10^{-5} / \text{K}$  for 1850 K-2900 K) is about 44 times larger than that of the fused silica ( $0.5 \times 10^{-6} / \text{K}$  for 1273 K) [32, 33]. The viscosity of liquid YAG ( $10^{4-5}$  mPa·s) is much lower than it of liquid fused silica ( $10^{10-11}$  mPa·s) and tremendous increase of YAG viscosity will occur once the temperature is lower than 400K. The surface tension of liquid YAG (0.81 N/m for 2073K) is higher than that of the liquid fused silica (0.307 N/m for 2073K) [34]. We argue that higher coefficient of thermal expansion and lower viscosity of liquid YAG material make the ejection process of molten material through the surface channel easier than liquid fused silica, and high surface tension feature has positive influence to liquid material maintaining sphere structure on surface. A sufficient amount of liquid fused silica can only be provided by the laser induced molten pool beneath the surface, where the larger pressure can overcome impedance. Smaller volume of molten YAG is enough to induce hemisphere on surface without the limitations caused by relatively high viscosity. Thus, hemisphere structures are more easily obtained in YAG and on small domains for micrometric sizes.

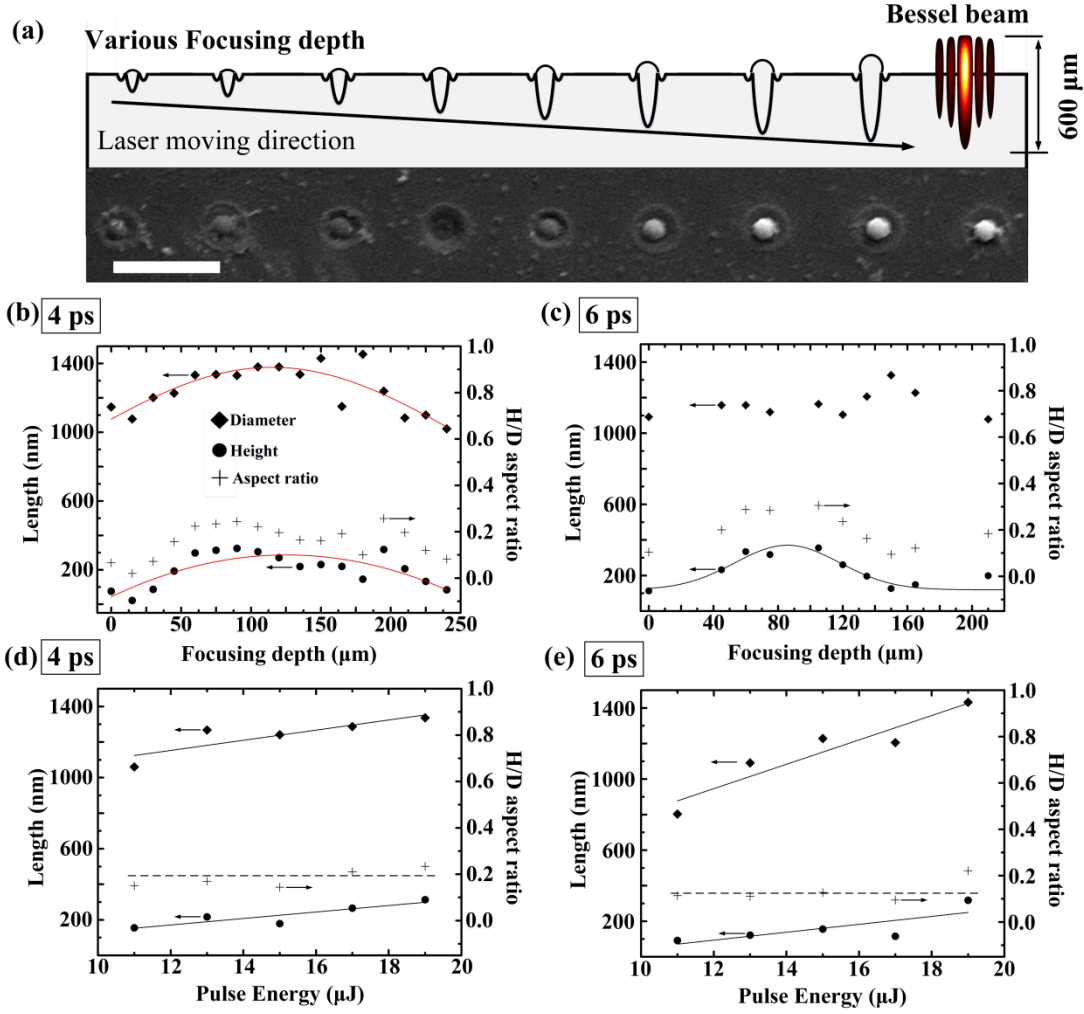


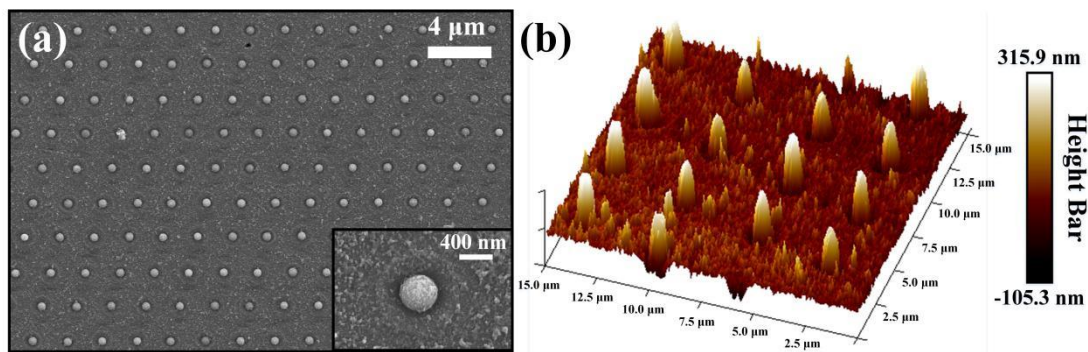
**Figure 3.** (a) Schematic and SEM images of hemisphere structure induced by 4 ps,  $91.57 \text{ J/cm}^2$  ( $17 \mu\text{J}$ ) single pulse Bessel beams processing at different focusing position. Scale bar is  $5 \mu\text{m}$ . Adjacent focusing depth difference is  $5 \mu\text{m}$ . Linear Bessel beam distribution is used to reveal approximate relative position. (b-c) Quantitative relationship between diameter, height, aspect ratio (Height/Diameter) and relative focusing depth (fixing single pulse energy to  $19 \mu\text{J}$  at all representation condition). We took the position where first hemisphere structure emerges as the relative depth zero position. (d-e) Quantitative relationship between diameter, height, aspect ratio and pulse energy (fixing focusing depth at the maximum intensity position of the beam at all representation condition). Solid lines and dotted lines are added to guide the eye and show the general trend of the curves.

Detailed morphology information of surface structure can be obtained by Atomic Force Microscopy (AFM). A  $300 \text{ nm}$  in height and  $1.3 \mu\text{m}$  in diameter single hemisphere structure, surrounded by a crater-like structure is observed. This typical aspect ratio is shown in Figure 3 b-e. A certain similarity can be observed with structures induced on metal films, with the exception that here the hemispherical forms are massive and there is no void inside [29,30]. Based on the topographical aspect we can associate the formation with the emergence and rapid cooling of liquid from the Bessel channel. This happens due to an internal pressure drive associated with an internal excitation and relaxation process that increase locally the pressure forcing the melting material to spill out to the surface through the hole. The inner part exposed to Bessel irradiation under ps conditions is often transformed into voids due to a local embedded cavitation process [35, 36]. At the threshold of the process the hydrodynamic expansion can be accurately controlled and

1 a hemisphere is constructed under effects of surface tension, expansion, cooling and solidification  
2 owing to its unique features mentioned above. At the limit of the processes, simple thermal  
3 expansion and stress release are sufficient to create convex structures on the surface. We will  
4 identify in the next paragraphs the processes pertinent in the present case.

5 The experimental results imply that the focusing position has a great influence on the  
6 morphology of the surface structures. SEM images in Figure 3a show the change of the structures  
7 when moving the focal plane position. The increment in the beam focusing position illustrated in  
8 the image is 5  $\mu\text{m}$ . Following a parametric study of varying depth and energy, relative  
9 relationships between the structure sizes (diameter and height) and laser parameters are  
10 summarized in Figure 3b-e. The adjusting of the Focusing depth has a non-monotonous effect on  
11 the size of the hemisphere. Here we define aspect ratio defined as Height / Diameter as a new  
12 parameter for morphology measurement. The height, diameter and aspect ratio increase first and  
13 then decrease with the beam focusing gets deeper. The diameter and height curves have a similar  
14 developing tendency as the longitudinal intensity distribution of Bessel beams [37]. The diameter  
15 of the structure induced by the 6 ps pulse changes more smoothly and the interval of relative  
16 focusing depth where hemispheres can be induced is smaller comparing to the 4 ps condition. One  
17 reason for this phenomenon is that the peak intensity of the 6 ps pulse is lower than the 4 ps pulse  
18 at the same pulse energy (19  $\mu\text{J}$ ). Since at 1030 nm the maximum peak intensity is achieved at the  
19 pulse duration of 1.5 ps around [38].

20 The smallest structure is induced by the 6 ps, 11  $\mu\text{J}$  ( $1,401 \text{ J}/\text{cm}^2$ ) pulse which is about 91  
21 nm high and 0.8  $\mu\text{m}$  in diameter. Aspect ratios notably remain lower than 0.2 for both 4 ps and 6  
22 ps condition, shown as dash lines in Figure 3b and c. Figure 3d-e reveals that the diameter and the  
23 height of the hemi-structure increase linearly when the pulse energy increase, while the aspect  
24 ratio is not sensitive to the energy change. The diameter of the hemisphere structure changes more  
25 rapidly with the increment of energy in the 6 ps pulse duration condition than that in the 4 ps  
26 situation. We expect that there will be a certain point where the linear increase trend ends and the  
27 hemisphere is replaced by crater. To sum up, the size of the hemisphere structures induced in air  
28 can be adjusted from 0.8  $\mu\text{m}$  to 1.4  $\mu\text{m}$  in diameter and 91 nm to 400 nm in height.



39  
40  
41  
42  
43  
44  
45  
46  
47  
48  
49  
50

**Figure. 4** (a) SEM images of large area hemisphere array with different magnification. Processing laser fluence is  $102.34 \text{ J}/\text{cm}^2$  with 4ps single pulse. The Period of the array is 4  $\mu\text{m}$ . (b) AFM image of the hemisphere array (15  $\mu\text{m} \times 15 \mu\text{m}$ ).

51  
52  
53  
54  
55  
56  
57  
58  
59  
60  
61  
62  
63  
64  
65

Based on high quality hemisphere structures and the effective processing parameters obtained above, we constructed large area hemisphere periodical array (more than 1 mm $\times$ 1 mm) on the surface of a YAG ceramic substrate using 4 ps, 19  $\mu\text{J}$  pulse ( $102.34 \text{ J}/\text{cm}^2$ ) beams and appropriate

focusing depth, as presented in Figure. 4a-b. Two SEM images with different magnifications are presented for a more detailed evaluation of the shape and size distribution of the hemisphere structures inside the array. The focusing depth of the laser beams was fixed when fabricated this array in order to maintain an identical size for the hemisphere structures. According to the AFM image shown in Figure 4c, the standard deviation of the height and the diameter are calculated as 24.05 nm (7%) and 58 nm (5.6%), respectively. The mean height is 325.4 nm and the mean diameter is 1034 nm. The homogeneity of this array shows a reproducibility of the hemisphere structure based on parameters control. Composite structures formed by hemisphere with different sizes therefore can be conducted.

## PLAL Results Discussion

In order to fully exploit the unique feature of the pulsed Bessel beam processing of transparent materials by controlling the surface matter evacuation pressure, the pulsed Bessel beam processing of YAG ceramic is now carried out in a liquid environment, with the purpose to analyze the role of the confinement environment on the quenching of the material ejection. The final Bessel beam after the imaging 4f system has a half-cone angle of 9.5 ° in water while the waist remains the same. This laser-liquid interaction on the substrate interface has a dual role, on one hand stabilizing the pressure above and, secondly, determining new interaction conditions by generating cavitation bubbles. Both the pressure gradient and the cavitation bubble on the interface are expected to influence the size and shape optimization of surface structures. The former can influence the material evolution on timescales related to bubble expansion or its collapse with the formation of micro-jets [36, 39].

Figure. 5a shows SEM images of hemisphere structures induced by single pulse Bessel beams with different parameters while the focusing depth was fixed. Compare to Figure 2a, it is remarkable that the hemisphere structures can be induced with much wider range of laser parameters under the assistance of water environment. The pulse duration interval relevant for the hemisphere production is optimized from 4- 6 ps without water to 0.2- 6 ps in the presence of water. The minimum efficient pulse energy is 7 μJ compared to 11 μJ in the air environment.

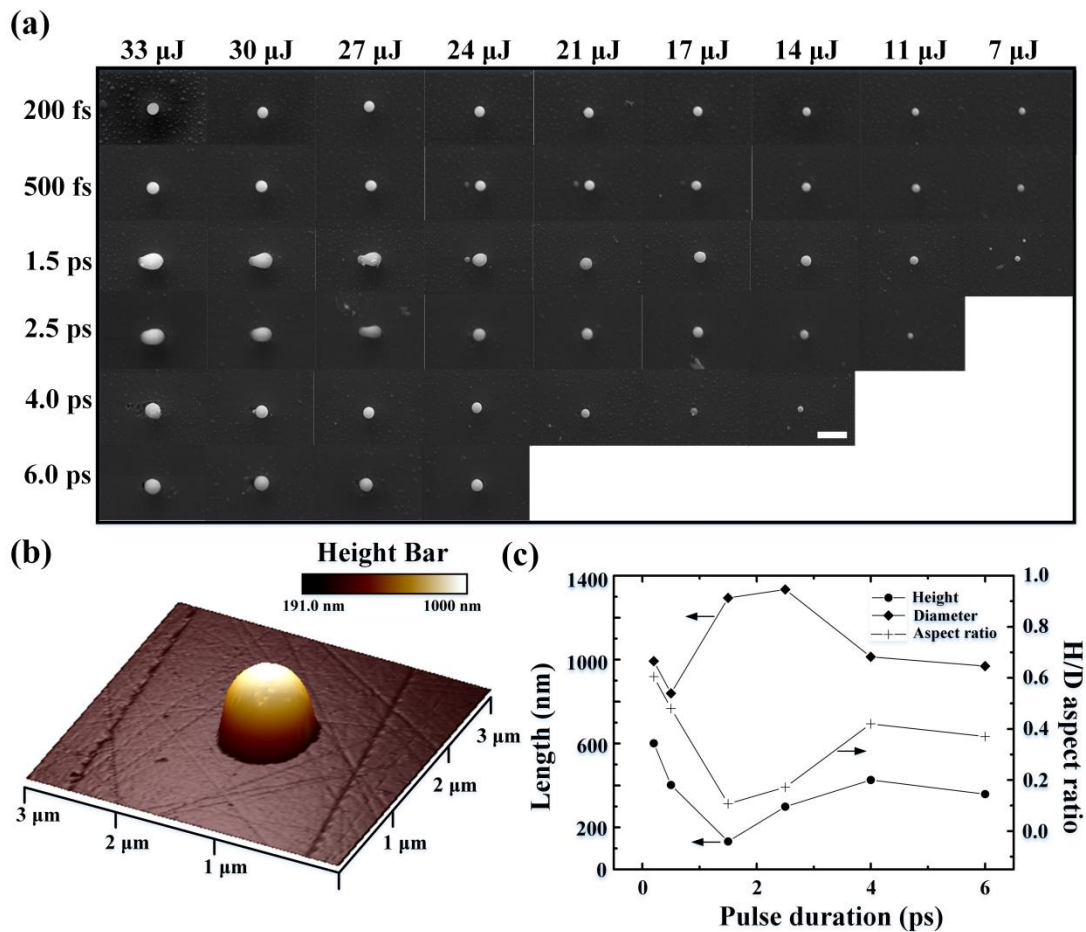
Concentric circle trenches corresponding to the Bessel rings cannot be observed under water when the pulse duration is less than 4 ps. We believe carrier excitation in water can distort the phase relation required for the ring formation. This leads to a spatial instability of the rings and therefore a smearing of energy density [39]. The Diameter and the associated morphology showing a high correlation with the pulse duration suggests a stronger effect for intermediate pulse durations. We recall that this effect is a combination of surface condition and pressure drive from beneath. The latter is maximized for slightly longer pulses with respect to the short ones as the nonlinear losses in the excited bulk are reduced [39,40]. A relation can also be set with the pulse energy, where the diameter of hemi-sphere increases with the energy.

Figure 5b represents a AFM figure of a hemisphere induced by femtosecond pulse laser. Three dimension morphology offers adequate data for us to analyse sphericity of hemisphere.

Sphericity of hemisphere structure can be written as  $S = \frac{3bc}{a^2} = \frac{3 \sqrt{Radiu1 \times Radiu2}}{Height^2}$  according to the definition [41]. Thus sphericity of hemisphere in Figure 5b can be calculated as 0.825 ( $S = 1$  represents the perfect spherical structure). The minimum sphericity of hemisphere induced in air condition can also be calculated as 1.73 which indicated liquid condition has positive effects on

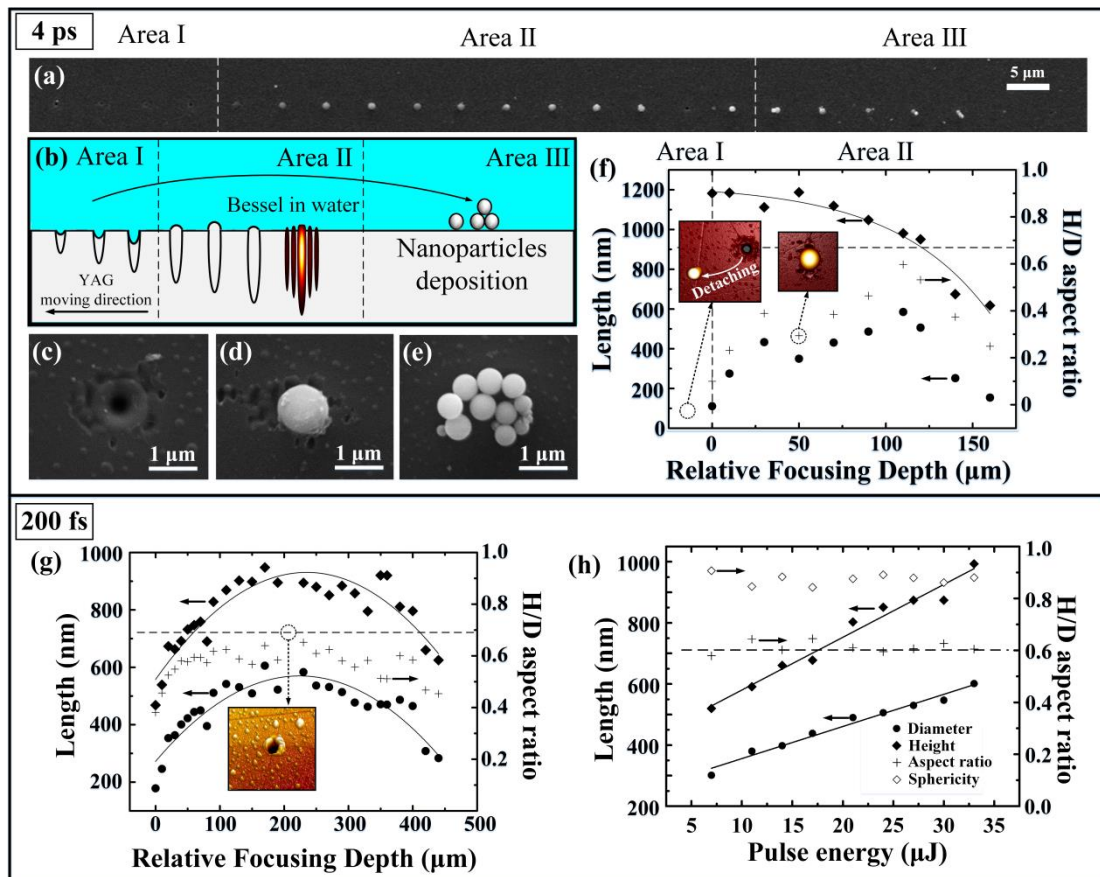
the improvement of structural sphericity.

Figure 5c summarizes the quantitative relationship between the size of the hemisphere structure (height, diameter and aspect ratio) and pulse duration when pulse energy is fixed as 33  $\mu\text{J}$ . Structures induced by 1.5 ps and 2.5 ps have an oval-shape, we take the mean value of the major and minor axis lengths as diameter. As we can see, the diameter increases first and then decrease as the pulse duration increases, reflecting again the different excitation efficiencies on the surface and in the bulk. Compared to the diameter evolution, the height and aspect ratio both show opposite curves. The 1.5 ps and 2.5 ps pulse duration cases in Figure 5a show high efficiency in inducing micro-structure on the interface at higher energies, with the hemisphere (ejected melt) becoming too big and the surface tension is not enough to hold the melt material inside. The liquid breaks apart before cooling and asymmetric structure formed. The mechanisms of micro-structure formation under liquid confinement is complex, being related both to flow properties and to the particular excitation geometry of the Bessel beam, where surface and volume are irradiated in a lapse of time of few ps, followed by bubble generation in the liquid above and in the material beneath [42,43].



**Figure 5.** (a) SEM images of hemisphere structures induced by single pulse Bessel beams with different laser parameters in the liquid environment (the focusing depth is fixed at around the maximum intensity region). The scale bar is 2  $\mu\text{m}$ . (b) AFM of a hemisphere induced by a single pulse of 33  $\mu\text{J}$  with 200 fs pulse duration. (c) Quantitative relationship between the size of the hemisphere structure (height, diameter, and aspect ratio) and the pulse duration. The fluence is fixed as 176.95  $\text{J}/\text{cm}^2$  (according to 33  $\mu\text{J}$ ).

1 The process of surface structure detaching and subsequent submicron particles deposition  
 2 was observed in the liquid-assisted processing experiment. Critical conditions for transition from  
 3 void structure, hemisphere and clusters of nanometer ball have been shown by SEM and AFM.  
 4 Figure. 6a shows an SEM image of different structures induced at different focusing conditions.  
 5 The laser beam parameters have been kept the constant: 4 ps, and 33  $\mu\text{J}$ . As the beam focusing  
 6 position changes, surface morphologies can be divided into three areas, as shown in Figure 6 a-b.  
 7 Area I is defined as where the micro-hole structures exist caused by surface structure detaching.  
 8 As beam focusing position gets deeper, Area II is where the hemisphere emerges. Its momentum  
 9 and kinetic energy seem not sufficient to detach and thus material remains on the surface, trapped  
 10 at the potential channel opening. Area III is the position where depositions of clusters of nanometer  
 11 ball are observed. The reconstructed Bessel beam distribution was used in order to show the  
 12 relative position between surface and laser intensity distribution. Considering refraction in the  
 13 YAG substrate, beam length can be estimated as about 1080  $\mu\text{m}$ . Figure. 6c-e shows typical  
 14 morphologies of three structures corresponding respectively to the three regimes. The damage  
 15 threshold in water is higher than in air. This can be related to additional losses generated by the  
 16 ignition of the plasma in water at irradiation levels well below those required to trigger the plasma  
 17 in air ( $10^{11-12}$  W/cm<sup>2</sup> compared to  $10^{13-14}$  W/cm<sup>2</sup>) [43,44].



55 **Figure 6.** (a) SEM images of surface micro-structures induced by 4 ps, 33  $\mu\text{J}$  pulse Bessel beams with different  
 56 focusing depths. (b) Schematic indication of various structures formation at different focusing conditions, defining  
 57 particular domains. (c-e) SEM images of different structures depicted as: submicron hole, hemisphere and  
 58 deposited micro-particles respectively. (f) Quantitative dependence of the size of Area II hemisphere structures  
 59  
 60  
 61  
 62  
 63  
 64  
 65

1 (height, diameter and aspect ratio) on the relative focusing depth. Area II and Area I are which are separated using  
2 a vertical dashed line. Pulse parameters are fixed as 4 ps and 33  $\mu\text{J}$ . AFM images show structure morphology at the  
3 corresponding depths. (g) Quantitative dependence of the size of Area II hemisphere structures on the relative  
4 focusing depth. AFM image shows a micro hole next to a hemisphere with aspect ratio of 0.65. Pulse parameters  
5 are fixed as 200 fs, 33  $\mu\text{J}$ . (h) Quantitative dependence of the size and sphericity of Area II hemisphere structures  
6 on the pulse energy. AFM image shows a hemisphere structures induced by single pulse Bessel beam with 200 fs  
7 and 33  $\mu\text{J}$ .  
8  
9

10  
11 Figure. 6f gives the quantitative relationship between the size of the hemisphere structures  
12 (height, diameter and aspect ratio) and the relative focusing depth. The position where the first  
13 hemisphere structure appears is defined as the zero position. The curve only shows the change of  
14 the hemisphere induced in Area II which are separated from Area I with a vertical dashed line. It  
15 can be revealed that the height-diameter aspect ratio first increase then decrease but not exceeding  
16 than 0.65. Considering the volume of laser material interaction region increases with beam focal  
17 depth increase, we argue that there is a possibility that more than one particle can detach from one  
18 irradiation position. After one particle detaching from the hole occurs, more melt material pours  
19 out from the micro hole and condense on the surface, as shown in right AFM image in the curve.  
20  
21

22  
23 Short pulse laser makes liquid assistance processing more efficient for generating hemisphere  
24 structures. A 200 fs pulse duration has been used in Figure 6g and h. Sphericity of hemisphere  
25 induced by 200 fs pulse laser have been demonstrated to be stable at 0.87 as shown in Figure 6h.  
26 The SEM and AFM images in Figure 5 and 6 reveal clean surroundings and a symmetric  
27 hemisphere structure with high surface quality and sphericity. The Diameter variation curve is  
28 similar to the intensity distribution of the Bessel beam. Laser intensity, according to plasma  
29 density is critical factor to generated the hemisphere structure. Considering the non-diffraction  
30 distance of focused Bessel beam is about 1080  $\mu\text{m}$  in YAG and 600  $\mu\text{m}$  in air, a structure-formable  
31 relative depth around 500  $\mu\text{m}$  is a large effective processing interval.  
32  
33

34  
35 Under 200 fs exposure, the smallest hemisphere has a diameter of 470 nm and a height of 180  
36 nm, while the biggest hemisphere is 606 nm high and 950 nm large in diameter. Therefore, the  
37 minimum and maximum aspect ratio induced by 200 fs in liquid environment are 0.38 and 0.64,  
38 which are much larger than aspect ratios of hemispheres induced in the air environment. The  
39 aspect ratio is strongly related to the processing environment, the beam focusing depth and the  
40 pulse duration. Hemisphere structures having aspect ratios lager than 0.65 will detach from the  
41 substrate surface and self-organize into a spherical particle in the liquid environment.  
42  
43  
44  
45  
46  
47  
48  
49  
50  
51  
52  
53  
54  
55  
56  
57  
58  
59  
60  
61  
62  
63  
64  
65

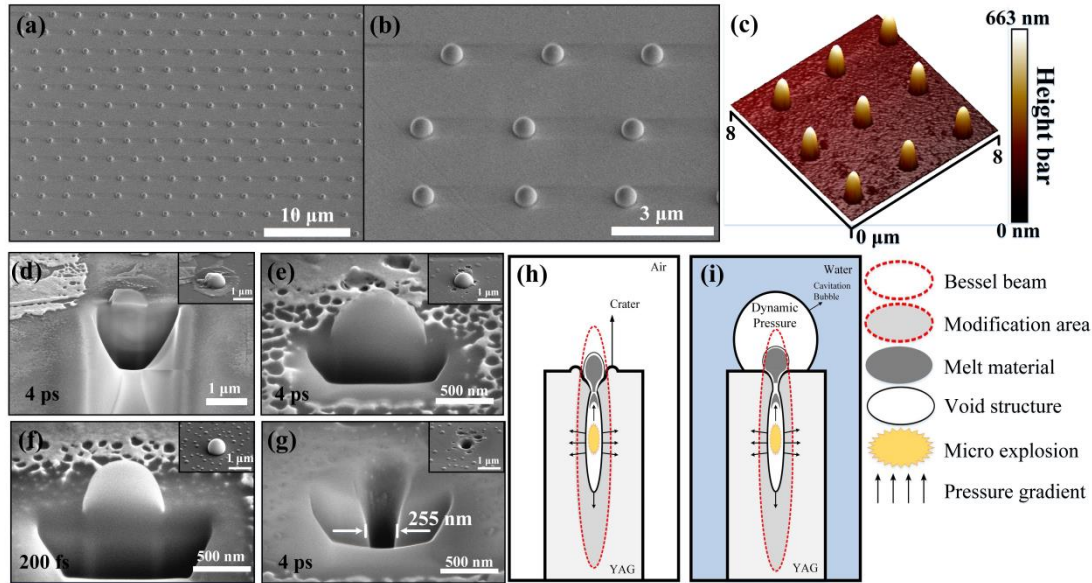


**Figure 7.** (a-b) are SEM images of a large area hemisphere array ( $1 \text{ mm}^2$ ) induced in water. Different magnifications are shown. Processing laser parameters are 200 fs,  $33 \mu\text{J}$ . The period of array is  $3 \mu\text{m}$ . The tilt angle of the image is  $42^\circ$ ; (c) AFM characterization image of hemisphere array ( $8 \mu\text{m} \times 8 \mu\text{m}$ ). (d-g) Side view images of micro-structures before and after FIB ablation. Tilt angle is  $52^\circ$ . Processing laser parameters are (d) 4 ps,  $19 \mu\text{J}$ , air conditions; (e) 4 ps,  $24 \mu\text{J}$ , water conditions; (f) 200 fs,  $33 \mu\text{J}$ , water conditions; (g) 4 ps,  $30 \mu\text{J}$ , water conditions, respectively. (h) Schematic of conventional laser ablation for fabricating particles in air using focused Bessel beams. (i) Schematic of pulse laser ablation fabricate hemisphere structures on YAG surface in water using focused Bessel beam. The legends illustrate the involved physical processes in the formation of hemisphere structures. Bessel beam region only refers to the central lobe of the beam.

This type of arrangement creates opportunities for large area processing with hemisphere on surface. As an example, a large area ( $1 \text{ mm}^2$ ) hemisphere array has been successfully fabricated under water irradiation condition using 200 fs,  $33 \mu\text{J}$  Bessel pulse beams while fixing the focusing position. Figure 7a-b show the SEM images with different magnification. The substrate is tilted for  $42^\circ$  in order to reveal the side profile. Combined with the detailed topography data obtained by AFM (Figure 7c), the standard deviation of the height and diameter were calculated as 12.44 nm (2.9 %) and 26.11 nm (3.0 %) respectively, while the mean height is 430 nm and mean diameter is 860 nm.

A focused ion beam (FIB) was used to reveal longitudinal morphology of the interior of the structures. Figure 7d-g show side views of the inner structure of two hemispheres induced by similar laser parameters in air and water environment, respectively. The inner structure of the hemisphere induced in air was revealed to be solid in a depth of more than  $1.5 \mu\text{m}$  rather than hollow. Despite of surrounding features (crater and voids) and different HD aspect ratio, the internal structures induced in air and water condition are both solid. This indicates that the hemisphere structure is formed from the solidification of the molten material ejected from the superficial regions through the channel.

The schematics of PLA and PLAL using Bessel single pulse beams are shown in Figure 7 h-i. The Bessel geometry with a long focusing depth implies that the interface and inner volume are irradiated by single pulse Bessel beam, at a picosecond period given by the projection of the

1 wavefront on the axis. Surface ablation and inner-volume modification can thus occur almost in  
2 the picosecond time range, much smaller compared to the hydrodynamic time [45]. Given the  
3 geometry the inner pressure relaxes on the direction of the strongest pressure gradient, i.e. radially.  
4 Channel structures can be induced in the vicinity of the surface. Surface opening may offer an  
5 additional relaxation path. This involves the whole thermomechanical evolution, from the pressure  
6 gradients to the liquid movement. However, when an opening is formed at the top of the channel,  
7 the relaxation direction will locally follow. The local pressure force melt material to eject through  
8 the channel to the surface at low speed and, upon cooling, hemisphere can thus be formed in the  
9 center of the ablation area. Thus it can be inferred that internal material absence can induce void  
10 structure below, as shown in Figure 7h-i. The formation of the hemisphere indicates also a  
11 relatively cold liquid with a higher viscosity.  
12

13  
14  
15 Additionally, the cavitation bubble (CB) that can be induced when the sample is immersed in  
16 water may have a non-negligible influence. Bessel beams with pulse duration less than 2.5 ps can  
17 only induce void and hole structures in air. The ability of fs duration pulse generating hemisphere  
18 in water indicates that that CB has a positive effect on molten material ejection, as shown in  
19 Figure 7i. The pressure in the bubble varies rapidly, so the temperature in the bubble change  
20 dramatically [46,47]. This effect may be related to rapid variations of the pressure and temperature  
21 within the bubble during their dynamics, which in turn will act on the cooling of the liquid and  
22 thus on its viscosity, but the effect stay for now speculative [46-48] The lifetime of CB has been  
23 demonstrated around 50-100  $\mu\text{s}$  (related to the size of the bubble) and 50 mg YAG particles can be  
24 solidify with rapid cooling rate within 6 seconds. The cooling rate is highly related to the sample  
25 weight and the spheroid structure is about  $5.14 \times 10^{-8} \mu\text{g}$ . Rapid cooling progress within CB  
26 lifetime thus can be inferred while direct experiment results are needed [47-49].  
27  
28  
29  
30  
31

## 32 CONCLUSIONS

33 We proposed a new method for fabricating various submicron structures in YAG ceramic by using  
34 ultra-fast single pulse non-diffractive Bessel beams in air and liquid environments. We show that  
35 the structure topography can be tuned from concave to convex forms by changing the focusing  
36 depth and the pulse duration. A type of highly regular hemisphere-shape surface micro-structures  
37 and submicron holes on YAG ceramic have been fabricated using this technique. Large area arrays  
38 of hemispheres with identical morphology were successfully fabricated in both air and water  
39 conditions. Cavitation bubble was demonstrated to have positive influence on the fabrication of  
40 surface hemisphere. Such organized arrays can find interest in optical applications and  
41 micro-photonics devices.  
42  
43  
44  
45  
46

## 47 Funding

48 This work was supported in part by the National Natural Science Foundation of China 61875226;  
49  
50

## 51 REFERENCES

- 52 [1] Glezer E N, Milosavljevic M, Huang L, et al. Three-dimensional optical storage inside transparent  
53 materials[J]. *Optics Letters*, 1996, 21(24):2023-2025.  
54 [2] Taylor R, Hnatovsky C and Simova E, Applications of femtosecond laser induced self-organized planar  
55 nanocracks inside fused silica glass. *Laser & Photon. Rev.*, 2008, 2: 26-46  
56 [3] Chanal, M., Fedorov, V. Y., Chambonneau, M. et al. Crossing the threshold of ultrafast laser writing in bulk  
57  
58  
59  
60  
61  
62  
63  
64  
65

silicon. *Nat Commun*, 773 (2017).

[4] Velpula P K, Bhuyan M K, Courvoisier F, Zhang H, Colombier J P, and Stoian R, Spatio-temporal dynamics in nondiffractive Bessel ultrafast laser nanoscale volume structuring, *Laser Photonics Rev.* 2016,10, 230-244.

[5] Stoian R, Colombier J P. Advances in ultrafast laser structuring of materials at the nanoscale[J]. *Nanophotonics*, 2020, 9. 10.1515.

[6] Zhang G, Cheng G, Bhuyan M, D'Amico C, Wang Y and Stoian R, Ultrashort Bessel beam photoinscription of Bragg Gratings waveguides and their application as temperature sensor, *Photonics Research*, 7(7), 2327 (2019)

[7] Hunt A J . Nanomorphing with Ultrafast Lasers and Biomedical Applications[J]. *MRS Online Proceeding Library Archive*, 2011, 1365.

[8] Hnatovsky C, Taylor R S, Simova E, et al. Polarization-selective etching in femtosecond laser-assisted microfluidic channel fabrication in fused silica[J] *Optics Letters*, 2005, 30: 1867–1869.

[9] Zorba V, Stratakis E, Barberoglou M, et al. Biomimetic Artificial Surfaces Quantitatively Reproduce the Water Repellency of a Lotus Leaf[J]. *Advanced Materials*, 2010, 20(21): 4049-4054.

[10] Lou R, Zhang G, Li G, Li X, Liu Q, Cheng G. Design and Fabrication of Dual-Scale Broadband Antireflective Structures on Metal Surfaces by Using Nanosecond and Femtosecond Lasers[J]. *Micromachines*, 2020, 11: 20.

[11] Marcinkevi A, et al. Femtosecond laser-assisted three-dimensional microfabrication in silica[J]. *Optics Letters*, 2001, 26(5): 277.

[12] Rgn A, Nnn A, Dbk B. Laser ablation of Ni in the presence of external magnetic field: Selection of microsized particles[J]. *Applied Surface Science*, 2020, 518.

[13] Zhang D, Gökce B, Barcikowski S. Laser Synthesis and Processing of Colloids: Fundamentals and Applications[J]. *Chemical Reviews*, 2017, 117(5): 3990 - 4103.

[14] Barcikowski S, Devesa F, Moldenhauer K. Impact and structure of literature on nanoparticle generation by laser ablation in liquids[J]. *Journal of Nanoparticle Research*, 2009, 11(8): 1883 - 1893.

[15] Dmitriy S, Ivanov, Rethfeld B, et al. The mechanism of nanobump formation in femtosecond pulse laser nanostructuring of thin metal films[J]. *Applied Physics A*, 2008, 92(4):791-796.

[16] Kuznetsov A I, Koch J, Chichkov B N. Nanostructuring of thin gold films by femtosecond lasers[J]. *Applied Physics A*, 2009, 94(2):221-230.

[17] Richter S, F Zimmermann, Eberhardt R, et al. Toward laser welding of glasses without optical contacting. *Applied Physics A*, 2015.

[18] Lorazo, P. , Lewis, L. J. , & Meunier, M. . (2003). Short-pulse laser ablation of solids: from phase explosion to fragmentation. *Physical Review Letters*, 91(22), 225502.,

[19] Colombier, J. P., Combis, P., Rosenfeld, A., Hertel, I. V., Audouard, E., & Stoian, R. (2006). Optimized energy coupling at ultrafast laser-irradiated metal surfaces by tailoring intensity envelopes: Consequences for material removal from Al samples. *Physical Review B*, 74(22), 224106.

[20] Cheng-Yu Shih, René Streubel, Johannes Heberle, Alexander Letzel, Maxim V. Shugaev, Chengping Wu, Michael Schmidt, Bilal Gökce, Stephan Barcikowski, Leonid V. Zhigilei, Two mechanisms of nanoparticle generation in picosecond laser ablation in liquids: the origin of the bimodal size distribution, *Nanoscale*, 2018, 10, 6900

[21] Vanagas, Egidijus, Kudryashov, et al. Surface nanostructuring of borosilicate glass by femtosecond nJ energy pulses. [J]. *Applied Physics Letters*, 2003.

[22] Shugaev, M., Wu, C., Armbruster, O., Naghilou, A., Brouwer, N., Ivanov, D., . . . Zhigilei, L. (2016). Fundamentals of ultrafast laser–material interaction. *MRS Bulletin*, 41(12), 960-968.

[23] Kuzmin P G , Shafeev G A , Serkov A A , et al. Laser-assisted fragmentation of Al particles suspended in

liquid[J]. *Applied Surface Science*, 2014, 294(mar.1):15-19.

[24] G Zhang, R Stoian, Wei Z, et al. Femtosecond laser Bessel beam welding of transparent to non-transparent materials with large focal-position tolerant zone[J]. *Optics Express*, 2018, 26(2): 917-926.

[25] Macdonald RP, Boothroyd SA, Okamoto T, et al. Interboard optical data distribution by Bessel beam shadowing[J]. *Optics Communications*, 1996, 122(4-6):169-177.

[26] Bouchal Z, Wagner J, Chlup M. Self-reconstruction of a distorted nondiffracting beam[J]. *Optics Communications*, 1998, 151(4-6): 207-211.

[27] Stoian R, Bhuyan MK, Zhang G, Cheng G, Meyer R, Courvoisier F. Ultrafast Bessel beams: Advanced tools for laser materials processing[J]. *Adv Opt Technol*, 2018, 7: 165 - 174.

[28] Velpula P K, Bhuyan M K, Courvoisier F, et al. Spatio-temporal dynamics in nondiffractive Bessel ultrafast laser nanoscale volume structuring[J]. *Laser & Photonics Reviews*, 2016, 10(2): 230 - 244.

[29] Dmitriy S, Ivanov, Rethfeld B, et al. The mechanism of nanobump formation in femtosecond pulse laser nanostructuring of thin metal films[J]. *Applied Physics A*, 2008, 92(4):791-796.

[30] Kuznetsov A I, Koch J, Chichkov B N. Nanostructuring of thin gold films by femtosecond lasers[J]. *Applied Physics A*, 2009, 94(2):221-230.

[31] MD Perry, Stuart B C , Banks P S , et al. Ultrashort-Pulse Laser Machining of Dielectric Materials[J]. *Journal of Applied Physics*, 1999, 85(9):6803-6810.

[32] Thermal Expansion of Yttrium Aluminum Garnet[J]. *Journal of the American Ceramic Society*, 1971, 54(7): 355-356.

[33] Pieter V, Erica B, Yves B. Local tuning of fused silica thermal expansion coefficient using femtosecond laser. *Phys. Rev. Materials*, 2019, 3, 053802, (2019)

[34] Feng S, Shan Z T , Pan R K , et al. Thermo-physical Property of YAG Melt Measured by Aerodynamic Levitation Technique[J]. *Journal of Inorganic Materials*, 2018.

[35] Bhuyan M K, Courvoisier F, Lacourt P A, Jacquot M, Salut R, Furfaro L, Dudley J M. High aspect ratio nanochannel machining using single shot femtosecond Bessel beams. *Appl Phys Lett*, 2010, 97(8): 081102.

[36] Faccio, D. , et al. Cavitation dynamics and directional microbubble ejection induced by intense femtosecond laser pulses in liquids. *Physical Review E* 86.3(2012):36304-36304.

[37] Chen T , Zhang G , Wang Y , et al. Reconstructing of Embedded High-Aspect-Ratio Nano-Voids Generated by Ultrafast Laser Bessel Beams[J]. *Micromachines*, 2020, 11(7).

[38] Guodong Zhang, Razvan Stoian, Rui Lou, Tianqu Chen, Guangying Li, Xu Wang, Yan Pan, Pengfei Wu, Jiang Wang, Guanghua Cheng, Thermal and mechanical limitations to processing resolution in volume non-diffractive ultrafast laser structuring, *Applied Surface Science*, 2021, 151170,

[39] Herbert E, Balibar S, Caupin F. Cavitation pressure in water [J]. *Physical Review E Statistical Nonlinear & Soft Matter Physics*, 2006, 74(4):041603.

[40] Bhuyan M K, Velpula P K, Colombier J P, et al. Single-shot high aspect ratio bulk nanostructuring of fused silica using chirp-controlled ultrafast laser Bessel beams. *Applied Physics Letters*, 2014, 104(2) : 219-377.

[41] Krumbein, W. C. Measurement and geological significance of shape and roundness of sedimentary particles. *Journal of Sedimentary Research* ,1941, 11(2), 64-72.

[42] Bhuyan M K, Antonin S, Madhura S, et al. High fidelity visualization of multiscale dynamics of laser-induced bubbles in liquids containing gold nanoparticles[J]. *Scientific Reports*, 2018, 8(1):9665.

[43] Shih C Y, Streubel R, Heberle J, et al. Two mechanisms of nanoparticle generation in picosecond laser ablation in liquids: the origin of the bimodal size distribution[J]. *Nanoscale*, 2018:10. 1039.C7NR08614H.

[44] Liu X L, Xin L, Liu X, et al. Tightly focused femtosecond laser pulse in air: from filamentation to breakdown[J]. *Optics Express*, 2010, 18(25):26007 - 26017.

- 1 [45] Stoian R, Bhuyan M K , Rudenko A , et al. High-resolution material structuring using ultrafast laser  
2 non-diffractive beams[J]. *Advances in Physics: X*, 2019, 4(1):1659180.
- 3 [46] W Soliman, et al. Modification of Rayleigh–Plesset Theory for Reproducing Dynamics of Cavitation  
4 Bubbles in Liquid-Phase Laser Ablation[J]. *Japanese Journal of Applied Physics*, 2010, 49(11):116202-116202.
- 5 [47] Wagener P, Schwenke A, Chichkov B N, et al. Pulsed Laser Ablation of Zinc in Tetrahydrofuran: Bypassing  
6 the Cavitation Bubble[J]. *Journal of Physical Chemistry C*, 2010, 114(17): 7618 - 7625.
- 7  
8 [48] Akhatov I, Lindau O, Topolnikov A, Mettin R, Vakhitova N, Lauterborn W. (2001). Collapse and rebound of  
9 a laser-induced cavitation bubble. *Physics of Fluids*, 13(10), 2805-2819.
- 10  
11 [49] Gervais M, et al. Crystallization of Y3Al5O12 garnet from deep undercooled melt effect of the AlGa  
12 substitution. *Materials Science & Engineering B* 45.1-3, 1997:108–113.
- 13  
14  
15  
16  
17  
18  
19  
20  
21  
22  
23  
24  
25  
26  
27  
28  
29  
30  
31  
32  
33  
34  
35  
36  
37  
38  
39  
40  
41  
42  
43  
44  
45  
46  
47  
48  
49  
50  
51  
52  
53  
54  
55  
56  
57  
58  
59  
60  
61  
62  
63  
64  
65